


 Cite this: *Chem. Commun.*, 2021, 57, 7168

 Received 18th May 2021,
 Accepted 22nd June 2021

DOI: 10.1039/d1cc02598h

rsc.li/chemcomm

NaBH₄-reduction induced tunable oxygen vacancies in LaNiO_{2.7} to enhance the oxygen evolution reaction†

 Yuwei Jin,^a Wenjing Huo,^a Libin Zhang,^b Yong Li,^c Qianqian Chen,^a Xiaodong Zhang,^a Shuo Yang,^{ad} Huagui Nie,^a Xuemei Zhou^{*a} and Zhi Yang^{ib} ^{*a}

Tunable oxygen vacancies of LaNiO₃ (LNO–Vo) are realized by theoretical prediction and the NaBH₄-reduction approach. The LNO_{2.7} catalyst exhibits superior catalytic activity and long-term stability for water oxidation. Direct evidence of the active site center and the intermediates is observed from *in situ* Raman spectra and DFT calculations.

Electrochemical water splitting is thought to be a promising technology to convert electrical energy into chemical fuels for hydrogen storage.¹ However, the oxygen evolution reaction (OER) significantly affects the overall water splitting efficiency owing to its sluggish kinetics and high overpotential.^{2,3} Noble metal oxides (such as RuO₂ or IrO₂) have been shown to be the most active OER electrocatalysts;⁴ however, their high cost and scarcity have greatly hindered their large-scale applications.⁵ Therefore, it is imperative to find low-cost alternative materials that can effectively decrease the kinetics limitation of the OER and improve the efficiency of water splitting. Non-precious-metal catalysts, such as perovskite oxides (ABO₃, where A is an alkaline- and/or rare-earth element and B is a transition metal element), have been considered as very promising candidates owing to the flexibility and tunability of their physicochemical and catalytic properties.^{6,7}

Generally, improved OER activity of ABO₃ can be achieved through manipulating the bond strength between the B-site species and the attached oxygenated species,^{8,9} optimizing the surface electronic structures.^{6,10,11} For instance, an adjustment of the oxygen vacancies (Vo) concentration can affect the OER activity.^{11,12} However, the perovskite oxides simultaneously

contain a complex mixture of charge, spin, orbitals, and defects that are strongly coupled.^{13,14} A slight change in one factor will significantly influence the others, which makes the structure–activity relationship of ABO₃ a complex issue that still requires further research. Therefore, the design and accurate synthesis of the perovskite oxide structure with excellent catalytic activity by defect engineering (such as the formation of oxygen vacancies) is of great significance for electrochemical water splitting.

LaNiO₃ (LNO) is very sensitive to oxygen stoichiometry.¹⁵ Herein, the structural models of the bulk LNO and LNO with Vo were first constructed using DFT (Fig. 1a and b and Fig. S1, ESI†). The number of lost oxygen atoms was designated as LNO_{2.83} (lost one oxygen atom), LNO_{2.67} (lost two oxygen atoms), and LNO_{2.5} (lost three oxygen atoms). As observed from Fig. 1c, the density of states (DOS) of the LNO system was continuous without any gap around the Fermi level, whereas the DOS of the LNO_{2.83} and LNO_{2.67} systems were negligible near the Fermi level. This indicated that LNO without Vo exhibited a metallic nature, and even a small change in Vo could induce metal–insulator transitions in the LNO system.^{16,17} This transition is closely related to the Ni 3d–O

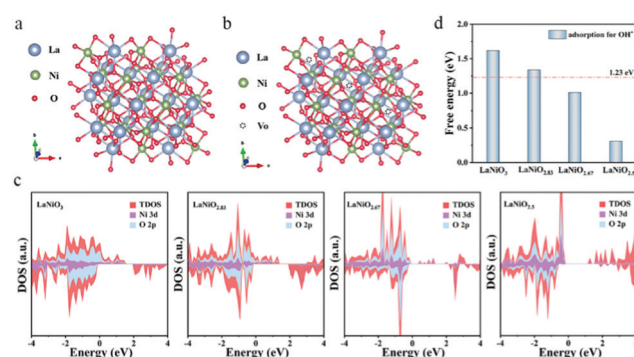


Fig. 1 The structure of the perfect LNO (a) and LNO with Vo (b); (c) the computed DOS of LNO, LNO_{2.83}, LNO_{2.67} and LNO_{2.5}, respectively; (d) the energy adsorption of OH* on the surface of LNO, LNO_{2.83}, LNO_{2.67} and LNO_{2.5} by DFT calculations.

^a Key Laboratory of Carbon Materials of Zhejiang Province, Wenzhou University, Wenzhou 325035, P. R. China. E-mail: zxm.mei@163.com, yang201079@126.com

^b Hangzhou Electric Connector Factory, Hangzhou, 310052, China

^c College of Mechanical and Electrical Engineering, Wenzhou University, Wenzhou, 325035, China

^d College of Electrical and Electronic Engineering, Wenzhou University, Wenzhou, 325035, China

† Electronic supplementary information (ESI) available. See DOI: 10.1039/d1cc02598h

2p hybridization strength, which will therefore be vital in adjusting the OER activity.¹⁷ Additionally, a suitable adsorption energy (1.23 eV) of OH* is valuable for increasing the reactivity of the active sites and the OER performance. The DFT calculations of the adsorption energy of OH* on the surfaces of LNO and LNO-Vo (Fig. 1d) indicated that the introduction of Vo in the LNO system promoted the adsorption of OH*, which might be beneficial for promoting the water oxidation kinetics. Therefore, these results implied that the optimal catalyst for the OER performance would be LNO having a concentration of Vo between those of LNO_{2.83} and LNO_{2.67}.

The as-prepared LNO by a sol-gel method was subjected to the NaBH₄-reduction method to synthesize LNO-Vo at room temperature (Fig. 2a). The concentration of Vo in the LNO products was controlled by the NaBH₄ reduction time (20 min, 30 min, and 1 h). X-Ray diffraction analysis (XRD) revealed that all of the prepared perovskites were in the hexagonal phase (PDF#34-1183), as shown in Fig. 2b. Compared with LNO, the XRD peak of LNO-Vo showed a noticeable shift toward a lower 2θ value, which suggested that Vo was introduced into the LNO system by the NaBH₄ treatment.¹⁸

The oxygen non-stoichiometry of LNO with NaBH₄ reduction times (20 min, 30 min, and 1 h) was calculated as

LNO_{2.85}, LNO_{2.7} and LNO_{2.54} (Fig. 2c) via the iodometric titration method,¹⁹ which indicated that accurate control of the Vo concentrations was achieved.

The as-grown products showed the morphology of the particles (Fig. 2d and Fig. S2, ESI†). The element mappings (Fig. S3, ESI†) further indicated the uniform distribution of La, Ni, and O in both the LNO_{2.7} and LNO particles. The lattice spacings were measured to be approximately 0.27 and 0.38 nm, which corresponded to the (110) and (101) facets of both LNO_{2.7} and LNO (Fig. 2e and f), in agreement with the XRD results. To identify the oxygen vacancies of LNO, high-angle annular dark-field scanning transmission electron microscopy characterization was carried out for LNO_{2.7}. In the line profiles of the angle annular dark-field scanning transmission electron microscopy micrographs along the white bars (Fig. 2g), the higher and lower fields were recognized as Ni and O atomic columns, respectively. The O sites are marked with black arrows in the Ni-O sequences. The oxygen vacancy concentrations were compared based on the absence of valleys at O sites (red arrows), which confirmed that the oxygen vacancies were successfully introduced into the bulk LNO.

The survey X-ray photoelectron spectroscopy (XPS) spectrum confirmed that all the as-grown products consisted of La, Ni and O elements (Fig. S4a, ESI† and Fig. 4d). As shown in Fig. 2h, the high-resolution O 1s spectra of all samples could be assigned with three peaks: the binding energy peak of a lattice oxygen (O_L) was at 528.6 eV, the peak of an oxygen vacancy (Vo) was at approximately 531.7 eV, and the peak of oxygen in the adsorbed water (H₂O) was at above 533.4 eV.^{19,20} An increased proportion of Vo was observed by increasing the NaBH₄ reduction time (Fig. 2h and Table S1, ESI†). Additionally, the Ni 2p_{3/2} peaks in LNO-Vo were slightly shifted to lower binding energies after the introduction of Vo, which suggested that the valence state of Ni was partly decreased (Fig. S4e, ESI†), which indicated that oxygen vacancies could adjust the electronic structure of Ni in LNO-Vo, and thereby affect the OER activities.

OER activities were tested in 1 M KOH solution and the linear sweep voltammetry (LSV) curves are presented in Fig. 3a. The current density of LNO_{2.7} over the whole potential range was higher than those of other catalysts (LNO, LNO_{2.85}, and LNO_{2.54}). Additionally, the overpotential of the LNO_{2.7} electrode at a current density of 10 mA cm⁻² was only 230 mV, which was much lower than those of the LNO (302 mV), LNO_{2.85} (268 mV), LNO_{2.54} (327 mV) and IrO₂ (277 mV) electrodes. The same tendency was also observed for all electrodes at each current density (Fig. S5, ESI†). As shown in Fig. 3b, the derived Tafel slope of 78 mV dec⁻¹ for LNO_{2.7} was much smaller than those for other catalysts (LNO, LNO_{2.85}, and LNO_{2.54}) and was reported in the range of 40–120 mV dec⁻¹ for Ni-based perovskite catalysts.^{21,22} In fact, the overpotential at 10 mA cm⁻² and the Tafel slope of LNO_{2.7} were superior to most of the reported Ni-based perovskite catalysts, as presented in Fig. 3c and Table S2 (ESI†).^{21–23} These results confirmed that the LNO_{2.7} electrode exhibits efficient kinetics for O₂ evolution.

The TOF values for the catalysts were calculated from the anodic current density at a specific overpotential. The TOF

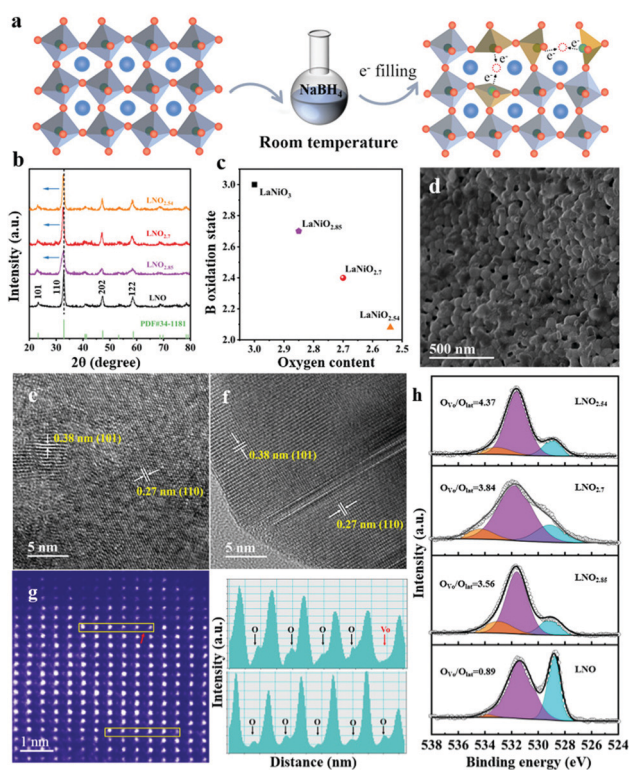


Fig. 2 (a) Schematic illustration of the synthesis of LNO-Vo by a room temperature reduction method; (b) XRD patterns of the as-grown samples; (c) the computed oxygen deficiency from the oxidation states of the Ni site in perovskite oxide materials by the iodometric titration method; (d) SEM images of LNO_{2.7}; TEM images of LNO_{2.7} (e) and LNO (f); (g) the left panel shows HAADF images of LNO_{2.7}; the right panel shows line profiles along the yellow bars in the HAADF images. (h) The high-resolution XPS spectrum of O 1s for LNO, LNO_{2.85}, LNO_{2.7} and LNO_{2.54}.

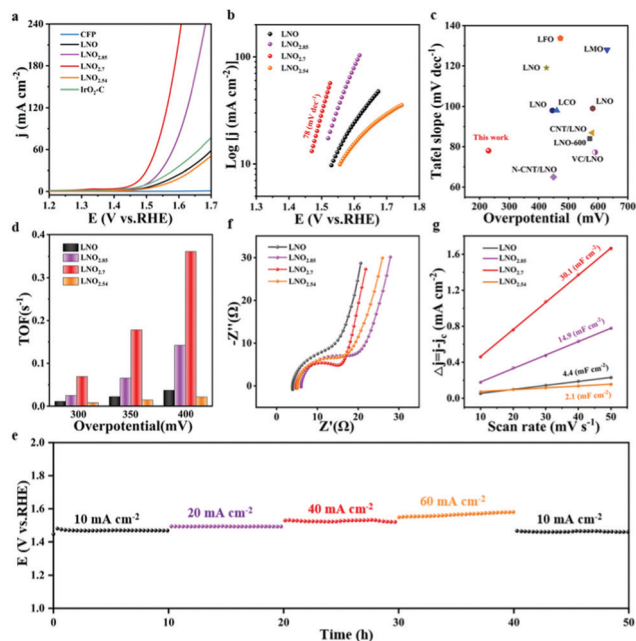


Fig. 3 (a) LSV of all catalytic electrodes in 1 M KOH with 90% iR corrections. (b) Tafel plots of four the catalysts corresponding to the LSV curves in (a); (c) the comparison of the OER activity with the overpotential at a current density of 10 mA cm^{-2} and Tafel slope; (d) the derived TOF values of four catalysts at different overpotentials, assuming all Ni atoms are active sites; (e) multi-current steps were also used to estimate stability with continuously varying current densities ($10, 20, 40, 60$ and 10 mA cm^{-2}). (f) Impedance Nyquist plots of LNO, LNO_{2.85}, LNO_{2.7}, and LNO_{2.54}; and (g) charging current density differences plotted versus scan rate.

value of LNO_{2.7} was 0.36 s^{-1} , which was much higher than those for LNO (0.04 s^{-1}), LNO_{2.85} (0.14 s^{-1}), and LNO_{2.54} (0.02 s^{-1}) under the same conditions at an overpotential of 400 mV (Table S1, ESI[†]). Moreover, the calculated TOF values of LNO_{2.7} at given applied potentials were much higher than those of the other LNO catalysts at the same potential, as presented in Fig. 3d. The TOFs of the LNO_{2.7} electrode also exhibited higher values than those of the previously reported Ni-based OER catalysts.^{24,25}

The stability of the LNO_{2.7} electrode was also estimated in a basic solution. There was no obvious attenuation of the LNO_{2.7} electrode over 25 h (Fig. S6, ESI[†]). Moreover, multi-current steps were also used to estimate the stability with continuously varying current densities. The potential of the LNO_{2.7} electrode at 10 mA cm^{-2} completely reverted to the initial values obtained at 10 mA cm^{-2} after measurements at various current densities, as shown in Fig. 3e. These results indicated that the LNO_{2.7} electrode is a promising OER catalyst with high activity and strong durability.

To gain insight into the reaction kinetics, electrochemical impedance spectroscopy (EIS) was conducted for the LNO electrodes. The typical Nyquist plots (Fig. 3f and Fig. S7, ESI[†]) indicated that the LNO_{2.7} electrode exhibited the lowest charge transfer resistance (R_{ct}) of 13.8Ω , where the measured R_{ct} values were 17.5Ω for LNO_{2.85}, 17.9Ω for LNO_{2.54}, and 22.4Ω for LNO. In the low frequency range of the Nyquist plots, the straight line corresponded to the Warburg resistance relative to

the diffusion of the electrolyte within the electroactive materials.¹¹ As observed from Fig. 3f, the slope of the LNO_{2.7} electrode was larger than those of other electrodes, which indicated an efficient chemical diffusion for the LNO_{2.7} electrode.

The electrochemically active surface area (ECSA) of all the catalysts was evaluated from the electrochemical double-layer capacitance (C_{dl}) based on the cyclic voltammetry (CV) method (Fig. S8, ESI[†]). The C_{dl} values of LNO_{2.85} (14.9 mF cm^{-2}) and LNO_{2.7} (30.1 mF cm^{-2}) were much higher than those of LNO (4.4 mF cm^{-2}) and LNO_{2.54} (2.1 mF cm^{-2}), as obtained from Fig. 3g, which indicated that the LNO electrode with oxygen defects possessed a larger electrochemically active surface area.

Raman spectroscopy can be used as a sensitive probe for the surface structure of the catalysts.²⁶ *In situ* Raman spectroscopy was adopted to reveal the active structure of the LNO_{2.7} and LNO electrodes during the OER process. As observed from Fig. 4, the LNO_{2.7} electrode at 1.37 V , where the OER commenced (LSV curves inset Fig. 4a), showed obvious Raman peaks at approximately 486 and 560 cm^{-1} , which corresponded to δ ($\text{Ni}^{\text{III}}\text{-O}$) and ν ($\text{Ni}^{\text{III}}\text{-O}$) vibrations of the NiOOH species, respectively (Fig. 4a).^{27,28} This implied that Ni would be an active site. The LNO electrodes formed the NiOOH species at 1.43 V (Fig. 4b), which indicated that the LNO_{2.7} electrode delivered a faster reaction process than that of the LNO electrode. Additionally, a broad band between 800 cm^{-1} and 1200 cm^{-1} appeared that was previously attributed to ν (O-O) of an active oxygen species (NiOO^-) in an oxyhydroxide structure (Fig. S9, ESI[†]). The *ex situ* XPS spectrum for the LNO_{2.7} electrode (Fig. S10 a and b, ESI[†]) showed that Ni 2p and Ni 3p spectral peaks were slightly shifted toward higher binding energies with the increase of the applied potential during the OER process, which implied that elemental Ni exhibited a higher valence state, thereby resulting in an enhanced OER performance, confirming the *in situ* Raman results.

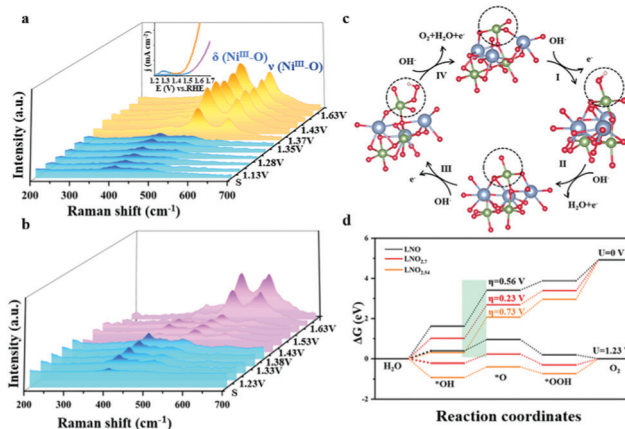


Fig. 4 *In situ* Raman spectra of (a) LNO_{2.7} (S refers to LNO_{2.7}) and (b) LNO (S refers to LNO_{2.7}) electrodes collected during LSV in alkaline solution; (c) a four-step OER mechanism on LNO_{2.7} in the alkaline electrolyte. The black dashed circle denotes the active site; (d) the calculated free-energy diagram for the OER over LNO, LNO_{2.7} and LNO_{2.54}, respectively.

The adsorption of intermediates (OH*, O*, and OOH*) on the catalysts was further investigated by the methanol probe molecule method.^{29,30} Fig. S11a–c (ESI†) shows the differences in LSV curves in the absence and presence of methanol for LNO, LNO_{2.7}, and LNO_{2.54}. The methanol oxidation reaction (MOR) current indicated that the surface coverage of OH* varied in the trend: LNO_{2.54} > LNO_{2.7} > LNO, which indicated that OH* adsorbed on LNO was looser than that on LNO_{2.7} and LNO_{2.54}, in agreement with the results of the adsorption energies of OH* by DFT calculations (Fig. 1d). The higher OER activity of LNO_{2.7} may originate from the relatively balanced bonding energy of OH*.

DFT calculations were carried out to gain in-depth understanding of the energetic OER pathway for the LNO_{2.7}, LNO and LNO_{2.54} systems.³¹ The optimized geometric structures of various intermediates along the reaction pathway are shown in Fig. 4c and Fig. S12 and S13 (ESI†), and the corresponding energy profiles are summarized in Fig. 4d. The rate-determining step (RDS) for the OER proceeding on a Ni site of LNO_{2.7} was the conversion of OH* to O* with a much lower overpotential of 0.23 V, compared with the pristine LNO (0.56 V) and LNO_{2.54} (0.73 V), which indicated a moderate O* adsorption at the Ni site for LNO_{2.7}. These results were in good agreement with the experimental measurements, where the introduction of suitable oxygen vacancies could adjust the Ni electronic state, and the LNO_{2.7} catalyst favoured the formation of the active species NiOOH and enhanced the bonding strength of intermediate OH* and O* adsorption at the Ni site, which in turn enhanced its OER activity.

Notably, the general applicability of controlling the Vo was also suitable for LaCoO₃ (LCO), LaMnO_{3.26} (LMO_{3.26}), and TiO₂ by the NaBH₄-reduction induced tunable oxygen vacancies approach (Fig. S14a–d, ESI†). Additionally, the OER catalytic activity of LCO_{2.9} and LaMnO_{3.14} was higher than those of LCO (Fig. S14e, ESI†) and LaMnO_{3.26} (Fig. S15, ESI†) based on the LSV curves. These above results indicated that this method could be generally used to control the oxygen vacancies and improve the catalytic activities.

In summary, we have successfully prepared LNO with accurate concentrations of oxygen vacancies by using the NaBH₄-reduction approach at room temperature. The LNO_{2.7} catalyst yields a current density of 10 mA cm⁻² at a low overpotential of 230 mV, which is accompanied by good stability under OER conditions. Direct evidence of the active site (Ni) and the intermediates (NiOOH species) is obtained from *in situ* Raman spectra, methanol probe molecule tests, and DFT calculations. This approach can also be generally used to control other compounds with oxygen vacancies (such as LaCoO₃, LaMnO_{3.26}, and TiO₂) for a variety of energy and storage conversion applications.

This work was supported in part by grants from the National Natural Science Foundation of China (51972238 and 21875166), Zhejiang Provincial Natural Science Foundation of China (LR18E020001 and LQ19B030006).

Conflicts of interest

There are no conflicts to declare.

References

- P. Strasser, *Acc. Chem. Res.*, 2016, **49**, 2658–2668.
- Z.-L. Wang, D. Xu, J.-J. Xu and X.-B. Zhang, *Chem. Soc. Rev.*, 2014, **43**, 7746–7786.
- X. Zhou, Z. Xia, T. Zhimin, Y. Ma and Y. Qu, *J. Mater. Chem. A*, 2015, **3**, 8107–8114.
- C. C. L. McCrory, S. Jung, I. M. Ferrer, S. M. Chatman, J. C. Peters and T. F. Jaramillo, *J. Am. Chem. Soc.*, 2015, **137**, 4347–4357.
- B. Hunter, H. Gray and A. Mueller, *Chem. Rev.*, 2016, **116**, 14120–14136.
- J. Suntivich, K. J. May, H. A. Gasteiger, J. B. Goodenough and Y. Shao-Horn, *Science*, 2011, **334**, 1383–1385.
- J. Hwang, R. R. Rao, L. Giordano, Y. Katayama, Y. Yu and Y. Shao-Horn, *Science*, 2017, **358**, 751–756.
- X. Xu, C. Su, W. Zhou, Y. Zhu, Y. Chen and Z. Shao, *Adv. Sci.*, 2016, **3**, 1500187.
- O. L. Malta, *Chem. Phys. Lett.*, 1982, **87**, 27–29.
- G. S. Hegde, A. Ghosh, R. Badam, N. Matsumi and R. Sundara, *ACS Appl. Energy Mater.*, 2020, **3**, 1338–1348.
- J. Kim, X. Yin, K. C. Tsao, S. Fang and H. Yang, *J. Am. Chem. Soc.*, 2014, **136**, 14646–14649.
- H. A. Tahini, T. Xin, U. Schwingenschlögl and S. C. Smith, *ACS Catal.*, 2016, **6**, 1157–1164.
- Y. Zhou, X. Guan, H. Zhou, K. Ramadoss, S. Adam, H. Liu, S. Lee, J. Shi, M. Tsuchiya, D. D. Fong and S. Ramanathan, *Nature*, 2016, **534**, 231–234.
- Z. Zhang, D. Schwanz, B. Narayanan, M. Kotiuga, J. A. Dura, M. Cherukara, H. Zhou, J. W. Freeland, J. Li and R. Sutarto, *Nature*, 2018, **553**, 68–72.
- M. T. Escote, F. M. Pontes, E. R. Leite, J. A. Varela, R. F. Jardim and E. Longo, *Thin Solid Films*, 2003, **445**, 54–58.
- R. D. Sánchez, M. T. Causa, A. Caneiro, A. Butera, M. Vallet-Regí, M. J. Sayagués, J. González-Calbet, F. García-Sanz and J. Rivas, *Phys. Rev. B: Condens. Matter Mater. Phys.*, 1996, **54**, 16574–16578.
- L. Qiao and X. Bi, *EPL*, 2011, **93**, 57002.
- J. R. Petrie, H. Jeon, S. C. Barron, T. L. Meyer and H. N. Lee, *J. Am. Chem. Soc.*, 2016, **138**, 7252–7255.
- K. Nam-In, S. Y. Jin, Y. T. Sup, C. S. Ryul, A. R. Arslan, C. Taekjib, S. Young-Soo, L. Kug-Seung, H. J. Yeon and C. W. Seok, *Sci. Adv.*, 2018, **4**, eaap9360.
- X. Zhou, Z. Tian, J. Li, H. Ruan, Y. Ma, Z. Yang and Y. Qu, *Nanoscale*, 2014, **6**, 2603–2607.
- R. P. Forsslund, W. G. Hardin, X. Rong, A. M. Abakumov, D. Filimonov, C. T. Alexander, J. T. Mefford, H. Iyer, A. M. Kolpak, K. P. Johnston and K. J. Stevenson, *Nat. Commun.*, 2018, **9**, 3150.
- Z. Li, L. Lv, X. Ao, J.-G. Li, H. Sun, P. An, X. Xue, Y. Li, M. Liu, C. Wang and M. Liu, *Appl. Catal., B*, 2020, **262**, 118291.
- J. G. Lee, J. Hwang, H. J. Hwang, O. S. Jeon, J. Jang, O. Kwon, Y. Lee, B. Han and Y.-G. Shul, *J. Am. Chem. Soc.*, 2016, **138**, 3541–3547.
- L. Han, S. Dong and E. Wang, *Adv. Mater.*, 2016, **28**, 9266–9291.
- S. H. Bae, J. E. Kim, H. Randriamahazaka, S. Y. Moon, J. Y. Park and I. K. Oh, *Adv. Energy Mater.*, 2017, **7**, 1601492.
- H. Kim, K. M. Kosuda, R. Dwyne and P. C. Stair, *Chem. Soc. Rev.*, 2010, **39**, 4820–4844.
- K. Zhu, X. Zhu and W. Yang, *Angew. Chem., Int. Ed.*, 2019, **58**, 1252–1265.
- P. W. Menezes, S. Yao, R. Beltrán-Suito, J. N. Hausmann, P. V. Menezes and M. Driess, *Angew. Chem., Int. Ed.*, 2021, **60**, 4640–4647.
- H. B. Tao, Y. Xu, X. Huang, J. Chen, L. Pei, J. Zhang, J. G. Chen and B. Liu, *Joule*, 2019, **3**, 1498–1509.
- W. Gou, M. Zhang, Y. Zou, X. Zhou and Y. Qu, *ChemCatChem*, 2019, **11**, 6008–6014.
- M. García-Mota, M. Bajdich, V. Viswanathan, A. Vojvodic, A. T. Bell and J. K. Nørskov, *J. Phys. Chem. C*, 2012, **116**, 21077–21082.